Nano Research Energy

ISSN 2791-0091 (print); 2790-8119 (online)
https://doi.org/10.26599/NRE.2026.9120235

Research Article

Confined interfacial microenvironment design of hard carbon anodes for wide-temperature sodium-ion batteries

Jiankun Wang[1], Peng Zhao[2], Qi Yang[1,4] (✉), Chenchen Yang[1], Yong Zhang[1], Puda Lu[1], Na Jiang[1], Yuhan Hao[1], Zhengjie Shang[1], Zhengbing Ren[1], Yifei Hou[1], Peng Huang[2], Xuejun Lu[1], Zhaodong Huang[3] (✉), and Jieshan Qiu[1,4] (✉)

[1] *State Key Laboratory of Chemical Resource Engineering, College of Chemical Engineering, Beijing University of Chemical Technology, Beijing* 100029, *China*
[2] *China Coal Research Institute Corporation Ltd., Beijing* 100013, *China*
[3] *Department of Chemical and Biological Engineering, Hong Kong University of Science and Technology, Clear Water Bay, Kowloon, Hong Kong* 999077, *China*
[4] *Liaoning Binhai Laboratory, Liaoning* 116051, *China*

Received: 6 March 2026 / **Revised:** 3 April 2026 / **Accepted:** 15 April 2026 / **Published date:** 21 May 2026

ABSTRACT

Low-concentration electrolytes hold significant potential for the development of cost-effective sodium-ion batteries (SIBs), whereas they face persistent challenges in sustaining the cycling stability of hard carbon anodes, especially under wide-temperature operation. This issue arises from the poorly controlled solid electrolyte interphase (SEI) formed in low-concentration electrolytes, typically featured by an inhomogeneous, fragile, and kinetically sluggish inorganic inner layer. Herein, we report a confined interfacial microenvironment design strategy by reconstructing a low-concentration ether electrolyte using a trace amount of anionic surfactant (sodium dodecyl sulfate, SDS). SDS is proposed to spontaneously adsorb and enrich at the hard carbon-electrolyte interface, creating a locally concentrated and confined interfacial microenvironment. Spectroscopic and electrochemical analyses indicate that this interfacial enrichment reshapes the local coordination/association environment of Na^+ during interfacial transport and desolvation, thereby promoting anion-involved interphase formation. This generates a thin SEI composed of an inner-layer rich in inorganic NaF and Na_2S and an organic out-layer, achieving a rigid-flexible integrated interphase to mitigate high-temperature interfacial instability and low-temperature sluggish kinetics. Consequently, the assembled SIBs show an improved cycling stability from a low capacity retention of 47.61% after 250 cycles to a high value of 91.44% after 350 cycles and demonstrate wide-temperature adaptability ranging from −15 to 50 °C. This study provides a promising interfacial microenvironment design strategy to address the instability challenge of hard carbon for high-performance wide-temperature SIBs.

KEYWORDS

sodium-ion batteries, low-concentration electrolyte, carbon materials, solid electrolyte interphase, wide-temperature operation

1 Introduction

Sodium-ion batteries (SIBs), benefiting from the natural abundance of sodium resources and intrinsic suitability for high-rate operation, are attracting intensive attention in the energy storage field [1–4]. As a crucial component of SIBs, the electrolyte is a primary determinant of electrode-electrolyte interface stability [5–8], especially across a wide-temperature range. The design of electrolyte components and their physicochemical properties governs the interface stability of hard carbon-based SIBs, primarily through controlling the chemistry and structure of the solid electrolyte interphase (SEI) formed on the hard carbon anode. Because SEI formation is highly temperature dependent [9–11], electrolyte design must simultaneously address two distinct interfacial constraints. At low temperatures, sluggish desolvation and charge transfer increase polarization; thus, an optimized electrolyte should promote the rapid formation of a compact, inorganic-rich SEI to facilitate Na^+ transport and mitigate capacity loss [12–16]. Conversely, at high temperatures, accelerated parasitic reactions can drive continuous electrolyte decomposition and uncontrolled SEI thickening. Therefore, electrolytes with high thermal and electrochemical stability are required to suppress side reactions, limit SEI overgrowth, and maintain the structural integrity of hard carbon, thereby ensuring cycling stability [17–21].

Address correspondence to Qi Yang, qi.yang@mail.buct.edu.cn; Zhaodong Huang, kezdhuang@ust.hk; Jieshan Qiu, qiujs@mail.buct.edu.cn

The regulation of electrolyte concentration is one of the key strategies for optimizing the stability of the electrolyte-electrode interface and enhancing the cycling performance and safety of batteries. Variations in concentration directly affect the solvation structure of the electrolyte, ionic transport characteristics, and the mechanisms of interface film formation, which in turn significantly influence the electrochemical stability, rate capability, and high-temperature tolerance of the battery. For high-concentration electrolytes (HCEs), when the salt concentration of NaFSI was increased to 5 M, the Ethylene Carbonate/Propylene Carbonate (EC/PC)-based electrolyte experienced rapid cell failure within 20 cycles because the high viscosity of EC/PC hindered charge transport and reduced ionic conductivity [22]. Choi et al. [22] instead used NaFSI in dimethoxyethane (DME), where the salt exhibits higher solubility, enabling the concentration to be increased to 5 M. They found that this electrolyte remained anodically stable up to 4.9 V vs. Na/Na^+. However, the large-scale application of HCEs in commercial SIBs remains challenging in the foreseeable future owing to the high cost of sodium salts, high viscosity, and poor wettability. For locally high-concentration electrolytes (LHCEs), adding inert diluents such as fluorinated ethers can reduce the viscosity of HCEs, thereby partially improving wettability and low-temperature conductivity. Fluoroether solvents meet these requirements and are therefore commonly used as diluents in LHCEs formulations. Symmetric fluoroether solvents, such as 1,1,2,2-tetrafluoroethyl-2,2,3,3-tetrafluoropropyl ether and bis(2,2,2-trifluoroethyl) ether (BTFE), have been employed in LHCEs [23–25]. Chou and co-workers [26] prepared HCEs consisting of 3.1 M NaTFSI in the trimethyl phosphate (TMP) and then diluted the mixture with the inert solvent BTFE to form LHCEs. Unfortunately, the addition of excessive BTFE disrupted the solvation balance in the original solution, leading to the recrystallization of NaTFSI in the electrolyte. Zhang et al. [27] used an LHCE of 2.1 M NaFSI/DME-BTFE (solvent molar ratio 1:2), which enables fast charging capability (20 C) and long cycling life (90.8% retention over 40,000 cycles) of $Na_3V_2(PO_4)_3$ cathodes. However, the high cost of commonly used fluoroether diluents restricts their practical application. Therefore, there is an urgent need to develop cost-effective diluents with favorable properties for LHCEs [28]. For conventional electrolytes, Xu et al. [29] used vinylene carbonate (VC) in an ether electrolyte, namely 1 M $NaPF_6$ in DME. They found that VC decomposed in large amounts on the surface of the electrodes into an excessively thick SEI with increased impedance. For low-concentration electrolytes, although researchers dissolved 0.8 M $NaPF_6$ in TMP solvent with 10% FEC additive to successfully achieve a non-flammable electrolyte, its initial Coulombic efficiency remains low at only 68.3% [30].

In contrast, low-concentration electrolytes exhibit unique advantages: First, the amount of salt used is significantly reduced, lowering costs by 20%–30% compared to conventional electrolytes; second, the high solvent content results in weak intermolecular forces, lower viscosity at ultra-low temperatures, and less resistance to ion migration, laying the foundation for high conductivity at low temperatures; third, low-concentration systems do not encounter issues related to salt aggregation, and the solvation structure can be precisely regulated through the incorporation of functional additives. This approach avoids diluent-induced interfacial perturbations and can, in principle, enable the concurrent realization of ultra-low temperature ionic conductivity, wide-temperature interface stability, and low cost [31]. However, pure low-concentration electrolytes have drawbacks such as weak SEI film formation ability, requiring functional additives for performance enhancement [32]. Functional additives, as an efficient strategy for electrolyte optimization, have become central to improving the overall performance of low-concentration electrolytes due to their small dosage and precise control [33]. Numerous studies have confirmed that the rational selection of additives can synergistically address the shortcomings of low-concentration electrolytes [34]. The electrolyte formulation of 0.35 M sodium bis (oxalato) borate (NaBOB) in the triethyl phosphate with the addition of 3 wt.% ethylene sulfate has been proposed, yet it exhibits rapid capacity fading when cycled at 55 °C and shows acceptable initial performance but undergoes a sharp decline in subsequent cycling stability at 40 °C. As a result, it fails to achieve long-term stable operation under high-temperature conditions. Moreover, its effect on improving battery performance is only limited to specific conditions such as room temperature and short-term cycling, thus featuring an extremely narrow application range [35]. Therefore, low-concentration electrolytes still face severe challenges in cycling stability under both high and low temperatures. Notably, for porous hard carbon electrodes, the decisive chemistry often occurs within a thin interfacial region and confined pores, where the local electrolyte environment can deviate substantially from the bulk composition, particularly under wide-temperature operation. This motivates an interfacial-centric design principle: trace additives can be made highly effective if they are capable of spontaneous enrichment at the hard-carbon surface, thereby reshaping local solvation/association and directing early-stage interphase formation.

In this work, we propose a confined interfacial microenvironment design strategy by introducing sodium dodecyl sulfate (SDS) as an anionic surfactant additive in low-concentration ether-based electrolytes. Owing to its spontaneous adsorption on hard carbon, SDS is expected to form an interfacial enrichment layer even at a low bulk dosage. When Na^+ traverses this interfacial layer prior to insertion, the accompanying anionic species can bias interfacial reactions toward anion-derived products and accelerate the formation of a thin, dense, inorganic-rich SEI, thereby stabilizing the interface across a wide temperature range. The interfacial-enrichment mechanism was demonstrated by nuclear magnetic resonance (NMR) spectroscopy and Raman spectroscopy. A thinner and more uniform SEI with an inorganic-rich inner layer was revealed through depth-resolved X-ray photoelectron spectroscopy (with sputter etching) and high-resolution transmission electron microscopy (HRTEM). As a result, the SDS-enabled low-concentration electrolyte delivers markedly enhanced reversible capacity, rate capability and cycling stability for hard carbon anodes, with the capacity retention improved from 47.61% after 250 cycles to a high of 91.44% after 350 cycles, and with stable operation further demonstrated across −15 to 50 °C. This interfacial-enrichment concept provides a practical and scalable route to reconcile low cost with wide-temperature stability in hard carbon-based SIBs.

2 Results and discussion

By employing advanced characterization techniques including NMR spectroscopy and Raman spectroscopy, the solvation structure and Na^+ coordination environment of a low-concentration electrolyte ($NaOTF_{0.5}$-G2, sodium salt, NaOTF, solvent, diglyme, G2) after the addition of SDS (0.03 M) were

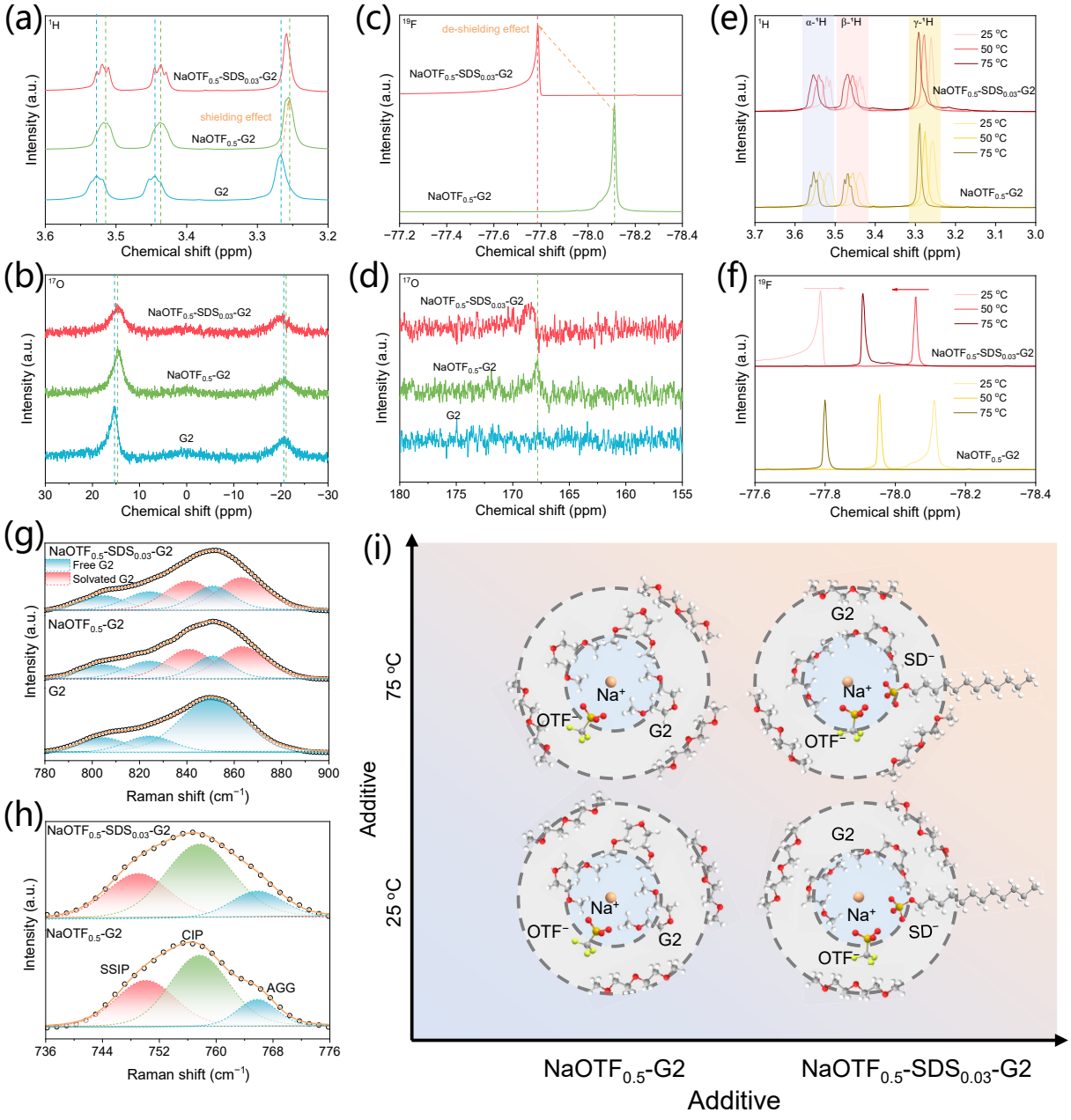

Figure 1 Solvation structure study of low-concentration electrolytes before and after using SDS additive. NMR spectra of (a) ^{1}H in G2, (b) ^{17}O in G2, (c) ^{19}F in two different electrolytes at 25 °C. (d) NMR of ^{17}O in NaOTF. NMR spectra of (e) ^{1}H and (f) ^{19}F in the two electrolytes at different temperatures. Raman spectra of different electrolytes at different Raman shift range of (g) free solvent G2 and Na^{+}-G2 coordination (780–900 cm^{-1}) and (h) OTF^{-} bending region (736–776 cm^{-1}). (i) Schematic diagram showing the temperature-dependent changes of solvation structure and coordination environment of low-concentration electrolytes with or without SDS additive.

elucidated. NMR data show that in bare solvent G2, both ^{1}H and ^{17}O-related signals shift upfield after introducing NaOTF (Figs. 1(a) and 1(b)), indicating enhanced electronic shielding that is consistent with salt-induced solvent structuring and strong Na^{+}-G2 coordination [36]. Adding 0.03 M SDS additive to the NaOTF$_{0.5}$-G2 electrolyte shifts both ^{1}H and O-related signals shift downfield, suggesting a re-polarization and de-shielding of the local solvent environment due to surfactant-mediated ionic nanodomains and competitive interactions involving the sulfate headgroups [37]. This indicates that SDS restructures the local solvation microenvironment and redistributes Na^{+} coordination/association equilibria, which can manifest as an apparent weakening of the average Na^{+}-G2 interaction in the bulk spectra [38]. Importantly, although SDS is introduced at a low bulk concentration, its anionic-surfactant nature enables spontaneous adsorption and enrichment at the hard carbon surface, creating an interfacial region with elevated sulfate density and a markedly different local electric field and ion-partitioning behavior from the bulk. The negative charge of the DS^{-} ion concentrates on the three oxygen atoms of the sulfate group. Although the long alkyl chain increases steric hindrance, the localized charge density enhances the electrostatic attraction with sodium ions [39]. Meanwhile, the negative charge of the OTF^{-} ion is highly delocalized through the three oxygen atoms of the sulfonic acid group and the strong electron-withdrawing effect of the trifluoromethyl group, leading to a dispersed charge density and weakening the binding with sodium ions. Therefore, the NMR signal of ^{19}F shifts downfield, resulting in a decrease in the electron cloud density around F atom

(de-shielding effect). Thus, the addition of SDS weakens the Na^+-OTF^- interaction (Fig. 1(c)). In Fig. 1(d), the downfield shift of the O-related signal, indicates a lower electronic shielding around oxygen, in line with the ^{19}F-NMR trend and the SDS-induced re-polarization of the solvation microenvironment. Taken together, these bulk-averaged NMR shifts are consistent with an SDS-induced reconstruction of the solvation structure via interfacial enrichment, local field effects, and competitive sulfate participation, which can be further amplified within the SDS-enriched interfacial layer where ion association and anion participation become more pronounced.

To elucidate the solvation structure changes caused by SDS [40], temperature- dependent NMR was used to obtain the molecular structure information of SDS in G2 solvent. With increasing temperature, in the $NaOTF_{0.5}$-G2 electrolyte system, the concentrations of α-^1H protons in G2 increased from 3.518, 3.438, 3.257 ppm at 25 °C to 3.533, 3.450, 3.272 ppm at 50 °C, and 3.547, 3.462, 3.284 ppm at 75 °C (Fig. 1(e)). The increments of α-^1H, β-^1H, and γ-^1H were 0.015, 0.012, 0.015 ppm from 25 °C to 50 °C and 0.029, 0.024, 0.027 ppm from 25 to 75 °C, respectively. This indicates that the coordination effect of Na^+-G2 weakens with increasing temperature, and the coordination effect of O (connected to α-^1H and γ-^1H) with Na^+ in G2 solvent is significantly smaller than that of (O connected to β-^1H). In the $NaOTF_{0.5}$-$SDS_{0.03}$-G2 electrolyte system, the concentrations of α-^1H protons in G2 increased from 3.519, 3.437, 3.258 at 25 °C to 3.533, 3.450, 3.274 ppm at 50 °C, and 3.545, 3.461, 3.285 ppm at 75 °C (Fig. S1 in the Electronic Supplementary Material (ESM)). The increases in α-^1H, β-^1H, and γ-^1H were 0.014, 0.013, 0.016, 0.026, 0.024, and 0.027 ppm, respectively. In the $NaOTF_{0.5}$-G2 electrolyte system, with increasing temperature, ^{19}F changed from −78.11 to −77.95 and −77.80 ppm, implying that increasing temperature leads to enhanced thermal motion and a greater distance between Na^+ and OTF^-, weakening the interaction between them. However, with adding SDS, ^{19}F decreased from −77.79 to −78.06 and −77.91 ppm (Fig. 1(f)), indicating that SDS increased the interaction between Na^+ and OTF^-. With increasing temperature, the interaction force between Na^+ and DS^- weakened (Fig. S2 in the ESM).

Raman spectroscopy was used to further study the solvation environment of Na^+. As shown in Fig. 1(g), bare G2 molecule exhibits three characteristic peaks at 804.7, 824.2 and 850.9 cm^{-1}, which are attributed to the coupling mode of its intramolecular $–CH_2–$ rocking vibration and C–O–C stretching vibration [41]. Correspondingly, when G2 coordinating with Na^+ to form a Na^+-G2 complex, its characteristic peaks appear at 840.9 and 863.2 cm^{-1} [42]. Quantitative analysis of the characteristic peak areas revealed that in the $NaOTF_{0.5}$-G2 basic electrolyte, the proportion of Na^+-solvated G2 was 38.43%. When adding SDS, this proportion decreased to 37.42% (Fig. S3 in the ESM). Rather than requiring extensive incorporation of SDS into the bulk solvation sheath, this subtle decrease suggests that the local coordination equilibrium experienced by Na^+ is shifted toward reduced solvent coordination, consistent with an adsorption-driven, anion-enriched interfacial microenvironment that accompanies Na^+ during interfacial transport and desolvation.

Simultaneously, we also analyzed the coordination environment of OTF^- anion. The characteristic peaks of OTF^- in the range of 736–776 cm^{-1} originate from its O–S–O bending vibration, which can be further divided into three different ion pair configurations (Fig. 1(h)). The peak at 749.0 cm^{-1} represents the solvent-separated ion pair (SSIP, uncoordinated free OTF^-), the peak at 757.6 cm^{-1} represents the contact ion pair (CIP, one OTF^- coordinated with one Na^+), and the peak at 765.8 cm^{-1} corresponds to the aggregate (AGG, one OTF^- coordinated with two Na^+) [43–45]. Quantitative fitting results showed that in the $NaOTF_{0.5}$-G2 basic electrolyte, the proportions of SSIP, CIP, and AGG were 34.57%, 52.33%, and 13.11%, respectively. However, after adding 0.03 M SDS, the proportions changed to 30.79% (SSIP), 54.52% (CIP), and 14.67% (AGG) (Fig. S4 in the ESM). These changes indicate enhanced ion association and a higher tendency for anion-cation contact states, which is particularly relevant for the confined interfacial region where SDS adsorption can create locally concentrated domains and promote anion-involved interfacial solvation/association during SEI formation.

Figure 1(i) schematically shows the chemical coordination environment of the electrolyte under different temperatures with or without SDS [46]. For the $NaOTF_{0.5}$-G2 baseline electrolyte, with increasing temperature, the enhanced molecular thermal motion leads to an increase in the distance between Na^+ and G2 solvent and OTF^-, resulting in a weakening of the interaction force between Na^+ and G2 solvent and between Na^+ and OTF^-. In contrast, for the $NaOTF_{0.5}$-$SDS_{0.03}$-G2 electrolyte, as the temperature increases, the coordination of Na^+ with G2 solvent and DS^- anions are weakened, while the interaction between Na^+ and OTF^- is enhanced. This temperature-dependent redistribution is proposed to occur predominantly within the SDS-enriched interfacial layer and confined pores, where local association states can be reshaped during Na^+ transport and desolvation. Therefore, DS^- and OTF^- enter the solvation sheath through competitive coordination, laying the foundation of SEI featured by an inner layer SEI rich in NaF and Na_2S on hard carbon.

Cyclic voltammetry (CV) curves show an improvement in rate capability with the addition of SDS. Across scan rates from 0.1 to 1 $mV·s^{-1}$, the $NaOTF_{0.5}$-G2 baseline electrolyte (Fig. 2(a)) shows weaker current responses, whereas the SDS-containing electrolyte (Fig. 2(b)) exhibits consistently higher current responses. Importantly, since a *b*-value closer to 0.5 indicates predominantly diffusion-controlled kinetics, whereas a *b*-value approaching 1.0 suggests a stronger surface/capacitive contribution, the two electrolytes both exhibit diffusion-dominated Na^+ storage behavior on hard carbon under the tested conditions. Notably, the SDS-containing electrolyte shows a moderately higher b value (0.5753 vs. 0.5401) (Fig. 2(c)) [47], indicating an increased contribution from faster surface-related processes and reduced kinetic constraints [48].

To quantitatively analyze this kinetic advantage from the perspective of interfacial processes, we performed electrochemical impedance spectroscopy (EIS) tests for the two electrolyte systems (Fig. 2(d)). It can be observed that all spectra consist of a semicircle in the high-frequency region and a diagonal line in the low-frequency region, corresponding to the charge transfer process and the solid-phase diffusion of Na^+ in electrode, respectively [49]. The charge transfer impedance (R_{ct}) value of the SDS-containing electrolyte is significantly lower than that of the baseline electrolyte. This result is highly consistent with the lower polarization observed in CV curves. In addition, the diffusion coefficient of Na^+ in the SDS-containing electrolyte is higher than that in the baseline electrolyte (Fig. S5(a) in the ESM). Considering that the ionic conductivity of the SDS-containing electrolyte is slightly increased (Fig. S5(b) in the ESM), it is proposed that SDS promotes the formation of a thinner, more uniform, and inorganic-rich SEI, which decreases the interfacial barrier for Na^+ desolvation/charge transfer and facilitates ion transport across the

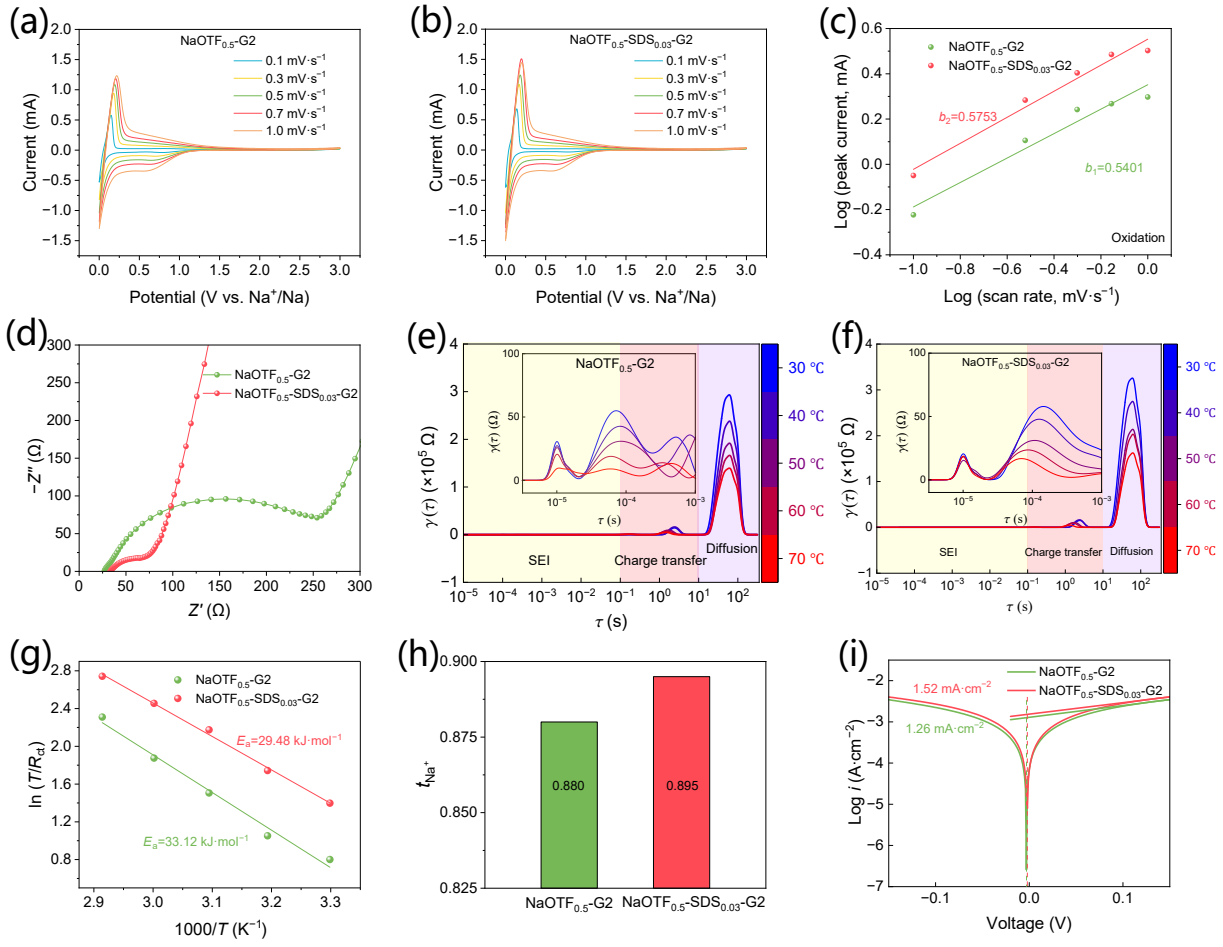

Figure 2 Interfacial kinetics of low-concentration electrolytes. CV curves of (a) $NaOTF_{0.5}$-G2, (b) $NaOTF_{0.5}$-$SDS_{0.03}$-G2 at different scan rates. (c) The *b*-value fitting curves based on CV data at different scan rates. (d) EIS of two electrolytes. DRT curves of (e) $NaOTF_{0.5}$-G2, (f) $NaOTF_{0.5}$-$SDS_{0.03}$-G2 the inset shows an enlarged view of the DRT spectra in the R_{SEI}-associated frequency region. (g) Desolvation energy of Na^+ desolvation derived from Nyquist plots. (h) Comparison of ion transference numbers, and (i) Tafel curves in low-concentration electrolytes with and without SDS.

interface, thereby lowering the overall impedance despite limited changes in bulk electrolyte properties.

To reveal the microscopic mechanism by which ether-based electrolytes influence the high and low temperature performance of hard carbon anodes from a kinetic perspective, relaxation time distribution (DRT) analysis was used to analyze the EIS data in the temperature range from 30 to 70 °C (Fig. S6 in the ESM). DRT successfully decoupled the conventional Nyquist plots of the $NaOTF_{0.5}$-G2 electrolyte (Fig. 2(e) in the ESM) and the $NaOTF_{0.5}$-$SDS_{0.03}$-G2 electrolyte (Fig. 2(f) in the ESM) into three independent processes, including ion migration in SEI (R_{SEI}), charge transfer (R_{ct}), and solid-phase diffusion (R_{diff}) [50]. By plotting the corresponding Arrhenius curves and calculating the activation energy, the baseline electrolyte exhibited a high activation energy (33.12 kJ·mol^{-1}) for the charge transfer process, while the value of the electrolyte containing SDS decreased to 29.48 kJ·mol^{-1} (Fig. 2(g)) [51]. This result indicates that SDS effectively reduces the energy barrier of Na^+ desolvation. The Na^+ transference number has increased from 0.880 to 0.895 (Fig. 2(h)). As shown in Fig. 2(i), a large stripping/electroplating exchange current density was achieved in an electrolyte containing SDS [52]. This is attributed to the anion-enhanced solvent induced by SD^- anions, which accelerates interfacial transport dynamics, consistent with the CV and impedance results above.

The impacts of electrolytes design on the layered composition, distribution profile of inorganic components, and micromorphology of the SEI on the hard carbon anode were comprehensively illustrated through a combination of XPS etching and HRTEM characterization techniques. SEI formed in two electrolytes were characterized in terms of chemistry and structure. XPS was used to analyze the chemical composition of SEI on hard carbon after cycling. The results showed that SEI formed in two electrolytes consist of similar elements (C, O, F, and S) (Figs. 3(a)-3(f)), while the contents show large differences. Specifically, for SEI formed in $NaOTF_{0.5}$-G2 electrolyte, four peaks can be fitted in the C 1s spectrum before Ar^+ etching, located at 284.8 eV (C–C), 286.6 eV (C–O–C), 288.3 eV (C=O), and 289.3 eV (Na_2CO_3) (Fig. S7 in the ESM) [53]. The signals at 533.4 and 532.2 eV in the O 1s spectrum can be attributed to $-CH_2-O-$ and C=O groups, corresponding to organic species generated by solvent reduction. In addition, the O 1s peak appearing at 531.2 eV corresponds to C–O–Na inorganic compounds (Fig. 3(a)). The F 1s spectrum shows distinct Na–F and C–F peaks at 684.1 and 688.9 eV, respectively (Fig. 3(b)), suggesting that they originate from the reductive decomposition of OTF^- anion. The S 2p spectrum shows peaks at 169.9, 168.7 eV (S $2p^{1/2}$, S $2p^{3/2}$, SO_4^{2-}), 168.4, 167.2 eV (S $2p^{1/2}$, S $2p^{3/2}$, SO_3^{2-}), and an S^{2-} peak at a lower binding energy (approximately 162.2 eV) (Fig. 3(c)), which originate from the reduction reaction of OTF^- [54, 55]. Although the XPS spectra of different systems have similar fitting peak positions, the relative contents of their organic and inorganic components are significantly different. With increasing etching

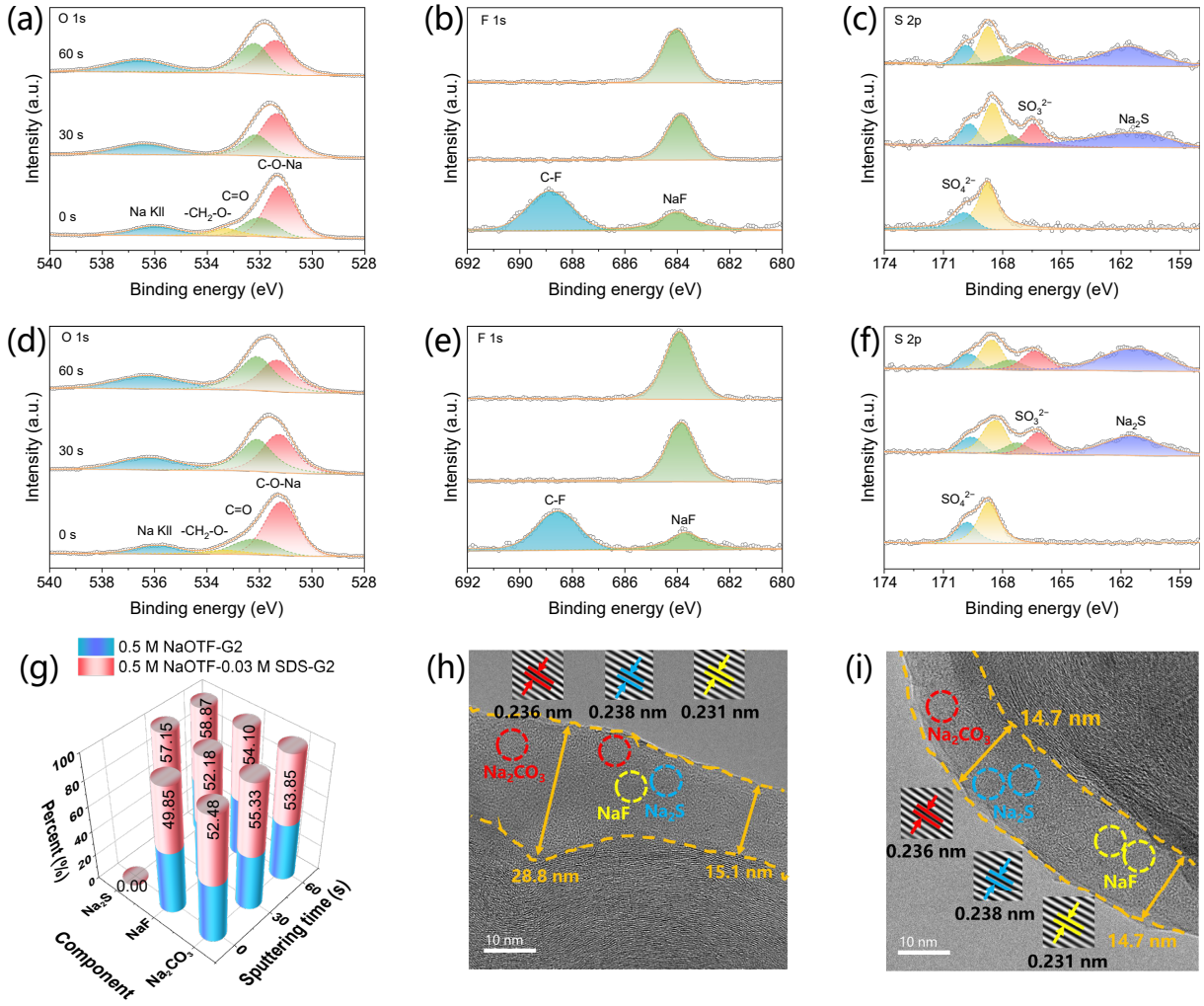

Figure 3 SEI characterization of Kuraray hard carbon anodes cycled in electrolytes with or without SDS. (a) O 1s, (b) F 1s, (c) S 2p XPS Spectra after cycling in $NaOTF_{0.5}$-G2 electrolyte, and (d) O 1s, (e) F 1s, (f) S 2p XPS Spectra after cycling in $NaOTF_{0.5}$-$SDS_{0.03}$-G2 electrolyte. The Ar^+ sputtering rate during XPS depth profiling was 0.2 nm·s^{-1}. (g) Statistical chart of the component contents of NaF, Na_2CO_3 and Na_2S. HRTEM images of hard carbon after 50 cycles in (h) $NaOTF_{0.5}$-G2 and (i) $NaOTF_{0.5}$-$SDS_{0.03}$-G2 electrolytes.

depth, compared to the $NaOTF_{0.5}$-G2 system, the SEI formed in $NaOTF_{0.5}$-$SDS_{0.03}$-G2 electrolyte contained lower organic components (C–C, C–O) (Fig. 3(d)), and a higher proportion of inorganic species, namely NaF (Fig. 3(e)) and Na_2S (Fig. 3(f)), which originate from the reduction reaction of OTF^- and DS^-. The types and relative proportions of inorganic components are summarized in Fig. 3(g).

The structure and morphology of SEI on hard carbon were further investigated using high-resolution electron microscopy. A 15.1–28.8 nm SEI with uneven thickness was observed on hard carbon cycled in $NaOTF_{0.5}$-G2 electrolyte (Fig. 3(h)). In contrast, in the $NaOTF_{0.5}$-$SDS_{0.03}$-G2 electrolyte, a more uniform SEI with a thickness of ~14.7 nm was observed on hard carbon (Fig. 3(i)). Moreover, SDS contributes to the formation of an inner-layer featured by a large amount of NaF and Na_2S, as supported by the corresponding data analysis (Fig. S8 in the ESM) [17]. Therefore, it can be inferred that the introduction of SDS promoted the preferential decomposition of anions, thereby facilitating the formation of a stable SEI rich in inorganic species.

The chemical composition and structure of the SEI on the hard carbon anode of SIBs, particularly the types and distribution of inorganic phases in the inner layer, are core factors determining the cycling stability and rate performance of the battery. Figure 4 illustrates the transport kinetics processes in low-concentration electrolytes with and without SDS, as well as the transport kinetics processes within the different SEI structures formed as a result. Distinct from conventional bulk-solvation tuning, the SDS additive perturbs the coordination/association equilibria of Na^+ in the ether electrolyte, as evidenced by the NMR and Raman signatures, indicating weakened Na^+-G2 coordination and a higher tendency toward anion-involved association states. Importantly, given the amphiphilic nature of SDS, we propose that its effect is amplified at the porous hard-carbon interface through spontaneous adsorption/enrichment, creating a locally concentrated and confined interfacial microenvironment that the charge carriers traverse prior to insertion. Such an interfacial environment favors anion-involved interphase chemistry during the initial cycles, thereby promoting the rapid formation of a thin, compact, and inorganic-rich SEI with a NaF/Na_2S-enriched inner layer as revealed by depth-resolved XPS and HRTEM. This early-stage formation of a robust inorganic inner layer effectively passivates the surface, suppresses continuous electrolyte consumption, and stabilizes the interface over extended cycling [56]. In contrast, the control sample, lacking such a directional inducer, experienced disordered reduction of electrolyte components, mainly generating a thick, loose, and organic-

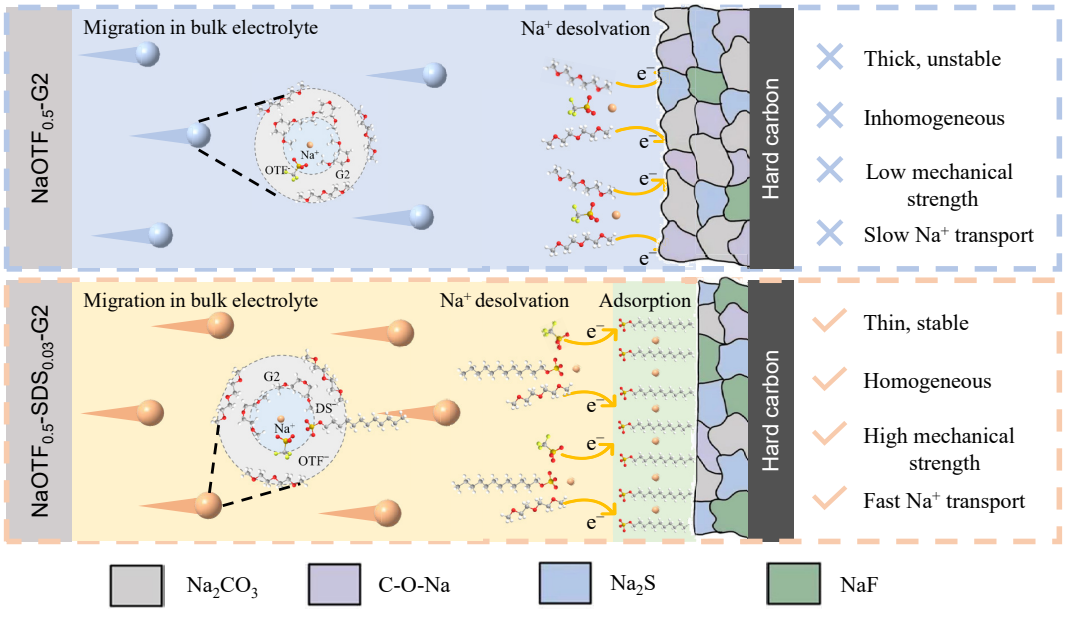

Figure 4 Schematic illustration of the kinetics processes of Na^+ transport and SEI structures derived from different electrolytes.

dominated undesirable SEI. Its inner layer lacked NaF [57], resulting in high interfacial impedance, persistent side reactions, and ultimately significant degradation of battery performance.

The electrochemical performances of low-concentration electrolytes with or without SDS were examined using commercially available Kuraray hard carbon under different temperatures. Based on the galvanostatic charge-discharge (GCD) curves of electrolyte systems with different SDS concentrations, 0.03 M SDS is determined as the optimal additive concentration (Fig. S9 in the ESM). At 25 °C, after introducing the SDS additive, the ICE of the hard carbon anode is increased from 91.76% in the baseline electrolyte to 92.64% in the SDS-containing electrolyte (Fig. S10 in the ESM). This is consistent with a more effective early-stage interphase formation in the presence of SDS, which reduces irreversible Na^+ consumption and improves the reversibility of the first cycle. The introduction of SDS enables excellent cycling stability at a low current density of 0.05 $A{\cdot}g^{-1}$, with a capacity retention of 90.98% after 80 cycles, which is much higher than that of the $NaOTF_{0.5}$-G2 electrolyte system (Fig. 5(a)). However, the capacity of the $NaOTF_{0.5}$-$SDS_{0.03}$-G2 electrolyte system exhibits a slight fluctuation during cycling, which is mainly attributed to uncontrolled ambient temperature drift during cycling. At a higher current density of 0.2 $A{\cdot}g^{-1}$, SDS significantly improves the cycling stability (Fig. 5(b)). The capacity retention rate increased from 50.01% after 250 cycles to 91.44% after 350 cycles. At high temperature (50 °C), the capacities of hard carbon in SDS-containing electrolyte reached 377.48 $mAh{\cdot}g^{-1}$ at 0.05 $A{\cdot}g^{-1}$ (Fig. 5(c)), with the initial Coulombic efficiency (ICE) improved from 93.46% to 94.37%, and 288.70 $mAh{\cdot}g^{-1}$ at 0.2 $A{\cdot}g^{-1}$ (Fig. 5(d)), higher than the baseline electrolyte (346.57 and 268.90 $mAh{\cdot}g^{-1}$). Moreover, SDS could also improve the cycling stability at high temperature. This is because that SDS can effectively regulate the interfacial solvation/association environment via adsorption-driven enrichment and promote more stable interphase formation at high temperatures. The low-temperature solubility of surfactants is a key factor determining low-temperature battery performance. The $NaOTF_{0.5}$-$SDS_{0.03}$-G2 electrolyte remained optically clear and homogeneous, showing no observable cloudiness or sedimentation after long-term storage at −15 °C (Fig. S11 in the ESM). At low temperature (−15 °C), SDS could also improve the cycling stability at different current densities of 0.05 and 0.2 $A{\cdot}g^{-1}$. At a current density of 0.05 $A{\cdot}g^{-1}$, the ICE is significantly improved from 83.80% to 87.54% with the SDS additive, and the capacity retention reaches 95.32% after 80 cycles (Fig. 5(e)). Meanwhile, at 0.2 $A{\cdot}g^{-1}$, a high capacity retention of 94.61% is achieved after 110 cycles (Fig. 5(f)). While decreasing temperature generally slows both reversible and parasitic processes, sub-ambient operation markedly aggravates kinetic limitations (e.g., desolvation/charge transfer) and increases interfacial polarization/resistance, which reduces the fraction of charge stored reversibly and renders irreversible interphase formation more prominent in the first cycle. The more pronounced ICE improvement at −15 °C therefore indicates that SDS more effectively regulates interphase formation and mitigates interfacial polarization under kinetically constrained conditions, consistent with the enhanced interfacial kinetics and the thinner, more uniform SEI revealed in our characterization. Therefore, under wide-temperature condition from −15 to 50 °C, SDS as an electrolyte additive can effectively optimize the interfacial solvation/association environment and significantly improve the reversible capacity, cycle stability and rate performance of hard carbon anodes (Fig. S12 in the ESM). To assess the compatibility of the electrolyte, modified asphalt YP50 was utilized as the hard carbon anode. At current densities of 0.05 $A{\cdot}g^{-1}$, the battery exhibited impressive capacity retention rates of 95.64% after 40 cycles (Fig. S13 in the ESM). This indicates that the designed electrolyte is highly effective in enhancing the cycling stability of SIBs. These findings further highlight the efficacy of the electrolyte and its potential for practical applications, particularly in prolonging battery lifespan and improving overall performance.

3 Conclusion

In summary, based on the confined interfacial microenvironment design strategy, SDS was utilized to regulate the interfacial solvation structure and interfacial properties of the low-concentration electrolyte, thereby constructing a "rigid-flexible integrated" SEI with a NaF-Na_2S-rich inner layer and an organic-rich outer layer. The effectiveness at a low bulk dosage is attributed

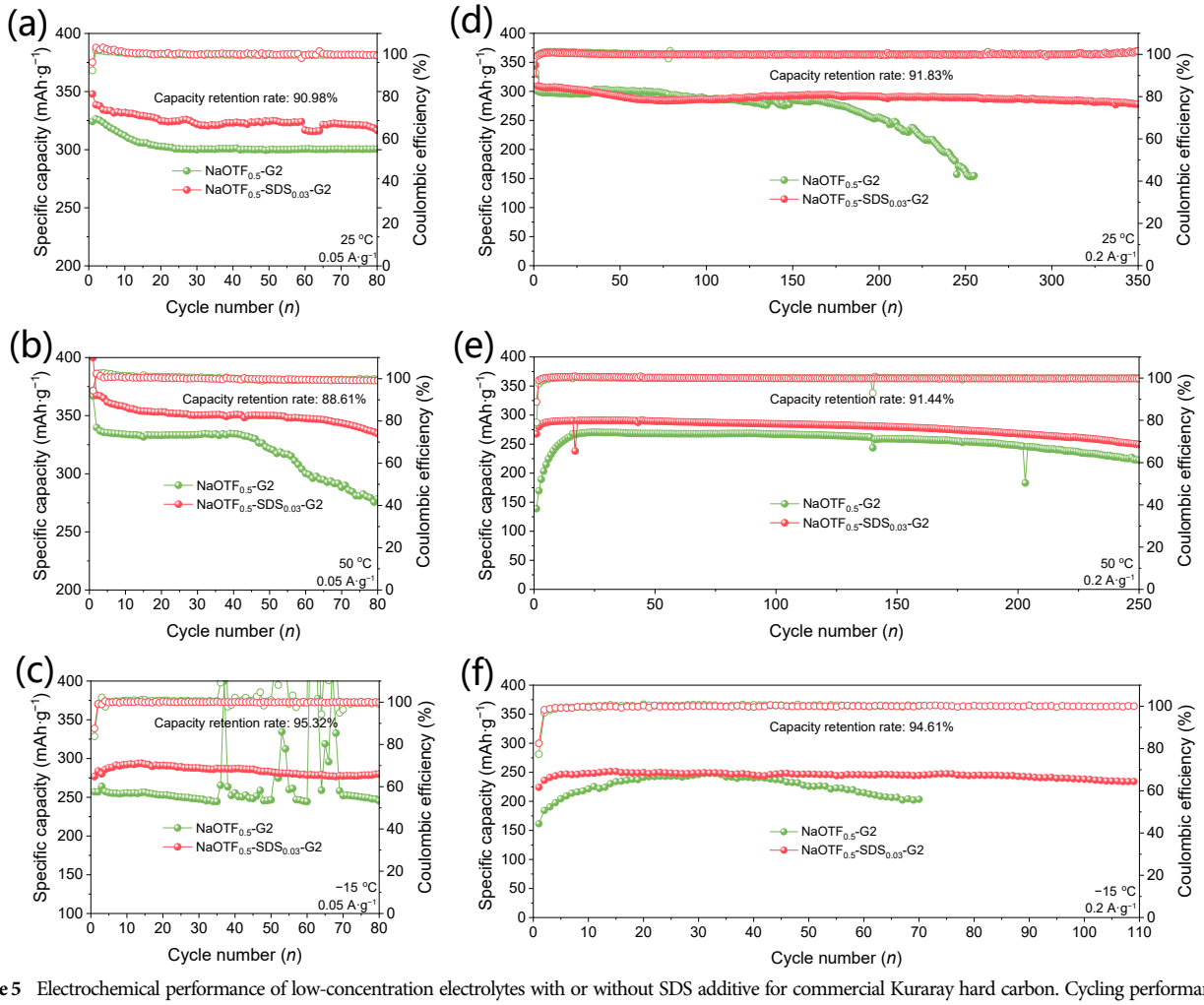

Figure 5 Electrochemical performance of low-concentration electrolytes with or without SDS additive for commercial Kuraray hard carbon. Cycling performance at (a) 0.05 A·g^{-1} and (b) 0.2 A·g^{-1} at 25 °C, at (c) 0.05 A·g^{-1} and (d) 0.2 A·g^{-1} at 50 °C, and at (e) 0.05 A·g^{-1} and (f) 0.2 A·g^{-1} at −15 °C in two different electrolytes.

to spontaneous adsorption and enrichment of the anionic surfactant on hard carbon, which creates a locally concentrated and confined interfacial microenvironment that directs anion-prioritized interphase formation. Combined with characterizations including NMR, Raman spectroscopy, etching XPS and TEM, this study elucidates the mechanism underlying SDS-induced reconstruction of the electrolyte interfacial solvation environment and clarifies the precise regulatory effect of interfacial phase engineering on the composition, structure and morphology of the SEI. The cycling stability was improved from a low capacity retention of 47.61% after 250 cycles to a high value of 91.44% after 350 cycles. The cycling stability enhancement was also demonstrated under wide-temperature conditions from −15 to 50 °C. This study provides a novel technical approach for the efficient compatibility of low-concentration electrolytes with hard carbon anodes, and it also offers important theoretical and experimental support for interfacial phase design and wide-temperature performance optimization of high-performance SIBs.

Acknowledgements

This work was financially supported by the Beijing Nova Program (20240484611), the National Natural Science Foundation of China (22393961, U23A20132), the fund by Liaoning Binhai Laboratory (LBLD-2025-02), the fund from China Coal Research Institute Corporation Ltd. (2024ZDI-05).

Declaration of conflicting interests

The authors declare no conflicting interests regarding the content of this article.

Data availability

All data needed to support the conclusions in the paper are presented in the manuscript and/or the Supplementary Materials. Additional data related to this paper may be requested from the corresponding author upon request.

Electronic Supplementary Material: Supplementary material (detailed electrolyte and pitch-derived hard carbon preparation procedures, Na^+ diffusion coefficient calculation formulas, solvation structure and interfacial kinetics data from NMR, Raman and EIS, SEI compositional and morphological analyses by XPS and TEM, 0.03 M optimal SDS concentration identification, and system wide-temperature performance and anode universality verification) is available in the online version of this article at https://doi.org/10.26599/NRE.2026.9120235.

References

[1] Li, Y. Q.; Vasileiadis, A.; Zhou, Q.; Lu, Y. X.; Meng, Q. S.; Li, Y.; Ombrini, P.; Zhao, J. B.; Chen, Z.; Niu, Y. S. et al. Origin of fast charging in hard carbon anodes. *Nat. Energy* **2024**, *9*, 134–142.

[2] Guo, Y. J.; Ji, S.; Wang, J. L.; Zhu, Z. Y.; Zhang, Y. J.; Xiao, J.; Liu, F.; Zeng, X. Y. Advancing hard carbon anode for sodium-ion batteries: Mechanisms and optimization strategies. *Nano Res. Energy* **2025**, *4*, e9120165.
[3] Zhang, Q.; Luan, J. Y.; Huang, X. B.; Wang, Q.; Sun, D.; Tang, Y. G.; Ji, X. B.; Wang, H. Y. Revealing the role of crystal orientation of protective layers for stable zinc anode. *Nat. Commun.* **2020**, *11*, 3961.
[4] Shi, Q. H.; Ning, F. H.; Yu, X.; Xia, F. J.; Qi, R. J.; Cheng, G. F.; Qiu, Y.; Liang, H. Y.; Zheng, H. F.; Zhang, T. et al. Decoupling slab gliding and lattice contraction in Na layered oxides to enable high-voltage Na-ion batteries. *Nat. Commun.* **2026**, *17*, 1516.
[5] Lu, Z. Y.; Yang, H. J.; Guo, Y.; Lin, H. X.; Shan, P. Z.; Wu, S. C.; He, P.; Yang, Y.; Yang, Q. H.; Zhou, H. S. Consummating ion desolvation in hard carbon anodes for reversible sodium storage. *Nat. Commun.* **2024**, *15*, 3497.
[6] Tian, Y. F.; Tan, S. J.; Lu, Z. Y.; Xu, D. X.; Chen, H. X.; Zhang, C. H.; Zhang, X. S.; Li, G.; Zhao, Y. M.; Chen, W. P. et al. Insights into anion-solvent interactions to boost stable operation of ether-based electrolytes in pure-SiO_x||$LiNi_{0.8}Mn_{0.1}Co_{0.1}O_2$ full cells. *Angew. Chem., Int. Ed.* **2023**, *62*, e202305988.
[7] Xiao, L. F.; Zeng, Z. Q.; Liu, X. W.; Fang, Y. J.; Jiang, X. Y.; Shao, Y. Y.; Zhuang, L.; Ai, X. P.; Yang, H. X.; Cao, Y. L. et al. Stable Li metal anode with "ion-solvent-coordinated" nonflammable electrolyte for safe Li metal batteries. *ACS Energy Lett.* **2019**, *4*, 483–488.
[8] Ding, X.; Yuan, W. W.; Lin, J. W.; Li, H. N.; Yang, X.; Liu, L. W.; Xiao, Y.; Chen, F.; Han, L. L. *In-situ* surface coating and subsurface gradient doping contrives P2-$Na_{0.67}Ni_{0.33}Mn_{0.67}O_2$ single crystal with highly stable interface and structure. *Nano Res. Energy* **2025**, *4*, e9120203.
[9] Yang, Q.; Jiang, N.; Li, X. X.; Zhi, C. Y.; Qiu, J. S. Electrochemical engineering in aqueous metal-ion batteries. *Sci. Bull.* **2025**, *70*, 2157–2172.
[10] Song, W. D.; Chen, N.; Wang, J. P.; Hua, W. B.; Zhang, B. H.; Zhao, S. Q.; Ming, X.; Shen, Z. X.; Chen, G.; Du, F. Mechanistic insights into enhanced capacity and pure-phase formation in Fe-based mixed phosphate cathodes. *J. Am. Chem. Soc.* **2025**, *147*, 39151–39159.
[11] Dong, X. R.; Zhang, Y.; You, Z. C.; Chen, Y. M.; Wu, X. W.; Wen, Z. Y. Polyanion-induced single Na-ion polymer electrolytes for ultra-stable sodium metal batteries. *Adv. Funct. Mater.* **2024**, *34*, 2405931.
[12] Liu, M. Q.; Wu, F.; Gong, Y. T.; Li, Y.; Li, Y.; Feng, X.; Li, Q. J.; Wu, C.; Bai, Y. Interfacial-catalysis-enabled layered and inorganic-rich SEI on hard carbon anodes in ester electrolytes for sodium-ion batteries. *Adv. Mater.* **2023**, *35*, 2300002.
[13] Chen, H.; Chen, K. A.; Yang, J. Y.; Liu, B. L.; Luo, L. B.; Li, H.; Chen, L.; Zhao, A. L.; Liang, X. M.; Feng, J. W. et al. Designing advanced electrolytes for high-safety and long-lifetime sodium-ion batteries via anion-cation interaction modulation. *J. Am. Chem. Soc.* **2024**, *146*, 15751–15760.
[14] Wang, X. Y.; Fan, Q.; Liu, Z. H.; Zhu, X. Y.; Yang, M.; Guo, Z. Y.; Chen, Y. T.; Wang, L. Q.; Jing, Y.; Xia, H. Anion-mediated approach to overcome oxidation in ether electrolytes for high-voltage sodium-ion batteries. *Nat. Commun.* **2025**, *16*, 2536.
[15] Guo, Z. Y.; Yang, M.; Fan, Q.; Chen, Y. T.; Xu, T.; Li, C. Y.; Li, Z. Y.; Li, Z. Y.; Sun, Q.; Xia, H. Inorganic-enriched solid electrolyte interphases: A key to enhance sodium-ion battery cycle stability?. *Small* **2024**, *20*, 2407425.
[16] Zhang, J.; Sawut, N.; Fan, H. M.; Li, Z.; Ai, X. P.; Fang, Y. J.; Cao, Y. L. Alleviating self-discharge in sodium-ion batteries via functional dual-salt electrolytes. *Nano Energy* **2025**, *136*, 110744.
[17] Ma, M. Y.; Cai, H. R.; Xu, C. L.; Huang, R. Z.; Wang, S. R.; Pan, H. L.; Hu, Y. S. Engineering solid electrolyte interface at nano-scale for high-performance hard carbon in sodium-ion batteries. *Adv. Funct. Mater.* **2021**, *31*, 2100278.
[18] Hu, C.; Dai, L.; Huang, F.; Yang, Y.; Liang, S. Q.; Fang, G. Z.; Zhang, Q. Carboxylate-based electrolyte with bilateral functions enable working sodium-metal batteries at –60 °C. *Angew. Chem., Int. Ed.* **2025**, *64*, e202508584.
[19] Chen, J. Y.; Dai, Z. Q.; Chen, H.; He, Z. D.; Dai, Y. C.; Shan, W.; Liu, W. H.; Wu, X. W.; Wen, Z. Y. Sodium-ion pump enhanced composite sodium anode toward fast-charging and practical N/P ratio solid-state sodium metal batteries. *Adv. Energy Mater.* **2025**, *15*, 2501061.
[20] Ren, Z. B.; Yang, Q.; Zhang, Y.; Lu, P. D.; Ma, Y.; Jiang, N.; Li, X. X.; Hao, Y. H.; Shang, Z. J.; Wang, J. K. et al. Structure engineering of coal pitch-derived hard carbon by molecular locking and multi-stage pore forming for enhanced sodium storage. *ACS Nano* **2026**, *20*, 7988–7999.
[21] Pei, Z. X.; Meng, Q. Q.; Wei, L.; Fan, J.; Chen, Y.; Zhi, C. Y. Toward efficient and high rate sodium-ion storage: A new insight from dopant-defect interplay in textured carbon anode materials. *Energy Storage Mater.* **2020**, *28*, 55–63.
[22] Lee, J.; Lee, Y.; Lee, J.; Lee, S. M.; Choi, J. H.; Kim, H.; Kwon, M. S.; Kang, K.; Lee, K. T.; Choi, N. S. Ultraconcentrated sodium bis(fluorosulfonyl)imide-based electrolytes for high-performance sodium metal batteries. *ACS Appl. Mater. Interfaces* **2017**, *9*, 3723–3732.
[23] Chen, S. R.; Zheng, J. M.; Mei, D. H.; Han, K. S.; Engelhard, M. H.; Zhao, W. G.; Xu, W.; Liu, J.; Zhang, J. G. High-voltage lithium-metal batteries enabled by localized high-concentration electrolytes. *Adv. Mater.* **2018**, *30*, 1706102.
[24] Jia, H.; Kim, J. M.; Gao, P. Y.; Xu, Y. B.; Engelhard, M. H.; Matthews, B. E.; Wang, C. M.; Xu, W. A systematic study on the effects of solvating solvents and additives in localized high-concentration electrolytes over electrochemical performance of lithium-ion batteries. *Angew. Chem., Int. Ed.* **2023**, *62*, e202218005.
[25] Xu, Y. B.; Jia, H.; Gao, P. Y.; Galvez-Aranda, D. E.; Beltran, S. P.; Cao, X.; Le, P. M. L.; Liu, J. F.; Engelhard, M. H.; Li, S. et al. Direct *in situ* measurements of electrical properties of solid-electrolyte interphase on lithium metal anodes. *Nat. Energy* **2023**, *8*, 1345–1354.
[26] Yang, Z.; He, J.; Lai, W. H.; Peng, J.; Liu, X. H.; He, X. X.; Guo, X. F.; Li, L.; Qiao, Y.; Ma, J. M. et al. Fire-retardant, stable-cycling and high-safety sodium ion battery. *Angew. Chem., Int. Ed.* **2021**, *60*, 27086–27094.
[27] Zheng, J. M.; Chen, S. R.; Zhao, W. G.; Song, J. H.; Engelhard, M. H.; Zhang, J. G. Extremely stable sodium metal batteries enabled by localized high-concentration electrolytes. *ACS Energy Lett.* **2018**, *3*, 315–321.
[28] Li, C. C.; Xu, H. Y.; Ni, L.; Qin, B. S.; Ma, Y. L.; Jiang, H. Z.; Xu, G. J.; Zhao, J. W.; Cui, G. L. Nonaqueous liquid electrolytes for sodium-ion batteries: Fundamentals, progress and perspectives. *Adv. Energy Mater.* **2023**, *13*, 2301758.
[29] Bai, P. X.; Han, X. P.; He, Y. W.; Xiong, P. X.; Zhao, Y. F.; Sun, J.; Xu, Y. H. Solid electrolyte interphase manipulation towards highly stable hard carbon anodes for sodium ion batteries. *Energy Storage Mater.* **2020**, *25*, 324–333.
[30] Zeng, Z. Q.; Jiang, X. Y.; Li, R.; Yuan, D. D.; Ai, X. P.; Yang, H. X.; Cao, Y. L. A safer sodium-ion battery based on nonflammable organic phosphate electrolyte. *Adv. Sci.* **2016**, *3*, 1600066.
[31] Li, Y. Q.; Yang, Y.; Lu, Y. X.; Zhou, Q.; Qi, X. G.; Meng, Q. S.; Rong, X. H.; Chen, L. Q.; Hu, Y. S. Ultralow-concentration electrolyte for Na-ion batteries. *ACS Energy Lett.* **2020**, *5*, 1156–1158.
[32] Yang, Y. J.; Yang, Y.; Yang, S. M.; Yao, Y.; Yang, Y.; Liu, L.; Rui, X. H.; Yu, Y. Dual-salt low-concentration electrolyte for low-temperature sodium metal batteries. *ACS Appl. Mater. Interfaces* **2025**, *17*, 22624–22632.
[33] Zhang, G. L.; Zhu, J. Q.; Wang, K.; Li, Q. R.; Fu, W. C.; Liu, X. X.; Sun, X. Q. A low concentration electrolyte additive for constructing solid-electrolyte interphase on a Zn metal anode for aqueous batteries. *Chem. Commun.* **2024**, *60*, 1317–1320.
[34] Kim, S.; Mirzapure, V.; Atwi, R.; Koppisetti, H. V. S. R. M.; Wasnik, K.; Rajput, N. N.; Shelke, M.; Pol, V. G. Insights into electrolyte-solvent interactions and SEI formation for sustainable sodium-ion battery operation at low temperatures. *Small Methods.*

2025, *9*, e02142.
[35] Welch, J.; Van Ekeren, W. W. A.; Mindemark, J.; Younesi, R. Effect of additives on the high-temperature performance of a sodium bis(oxalato)borate in triethyl phosphate electrolyte in sodium-ion batteries. *Chem. Commun.* **2025**, *8*, 127.
[36] Wang, X. Y.; Yang, C.; Yao, L. B.; Wang, Y. C.; Jiang, N.; Liu, Y. Anion/cation solvation engineering for a ternary low-concentration electrolyte toward high-voltage and long-life sodium-ion batteries. *Adv. Funct. Mater.* **2024**, *34*, 2315007.
[37] Zhang, Y. R.; Li, F.; Cao, Y.; Yang, M.; Han, X. P.; Ji, Y.; Chen, K. Z.; Liang, L. X.; Sun, J.; Hou, G. J. Tuning the FEC-related electrolyte solvation structures in ether solvents enables high-performance lithium metal anode. *Adv. Funct. Mater.* **2024**, *34*, 2315527.
[38] Wang, G. Y.; Fu, H.; Lu, J.; Huang, S. Y.; Pei, C. G.; Min, D.; Zhang, Q.; Park, H. S. Gradient-structured and robust solid electrolyte interphase *in situ* formed by hydrated eutectic electrolytes for high-performance zinc metal batteries. *Adv. Energy Mater.* **2024**, *14*, 2303549.
[39] Eliasquevici, R.; Bernardino, K. Counter-ion adsorption and electrostatic potential in sodium and choline dodecyl sulfate micelles–a molecular dynamics simulation study. *J. Mol. Model.* **2024**, *30*, 101.
[40] Xia, Y. C.; Zhou, P.; Kong, X.; Tian, J. K.; Zhang, W. L.; Yan, S. S.; Hou, W. H.; Zhou, H. Y.; Dong, H.; Chen, X. X. et al. Designing an asymmetric ether-like lithium salt to enable fast-cycling high-energy lithium metal batteries. *Nat. Energy* **2023**, *8*, 934–945.
[41] Zhou, X. Z.; Huang, Y. H.; Wen, B.; Yang, Z.; Hao, Z. Q.; Li, L.; Chou, S. L.; Li, F. J. Regulation of anion-Na^+ coordination chemistry in electrolyte solvates for low-temperature sodium-ion batteries. *Proc. Natl. Acad. Sci. USA* **2024**, *121*, e2316914121.
[42] Li, S. Q.; Song, X. R.; Jing, P. W.; Xiao, X. Y.; Chen, Y. C.; Sun, Q.; Huang, M. X.; Zhang, Y. P.; Li, G. S.; Liu, P. Y. et al. Trace $NaBF_4$ modulated ultralow-concentration ether electrolyte for durable high-voltage sodium-ion batteries. *Adv. Funct. Mater.* **2025**, *35*, 2422491.
[43] Cao, Z.; Zheng, X. Y.; Qu, Q. T.; Huang, Y. H.; Zheng, H. H. Electrolyte design enabling a high-safety and high-performance Si anode with a tailored electrode-electrolyte interphase. *Adv. Mater.* **2021**, *33*, 2103178.
[44] Wu, J. R.; Gao, Z. Y.; Tian, Y.; Zhao, Y.; Lin, Y. L.; Wang, K.; Guo, H. X.; Pan, Y. F.; Wang, X. S.; Kang, F. Y. et al. Unique tridentate coordination tailored solvation sheath toward highly stable lithium metal batteries. *Adv. Mater.* **2023**, *35*, 2303347.
[45] Jiang, Z. P.; Zeng, Z. Q.; Zhang, H.; Yang, L.; Hu, W.; Liang, X. M.; Feng, J. W.; Yu, C.; Cheng, S. J.; Xie, J. Low concentration electrolyte with non-solvating cosolvent enabling high-voltage lithium metal batteries. *iScience* **2022**, *25*, 103490.
[46] Verma, V.; Chan, R. M.; Yang, L. J.; Kumar, S.; Sattayaporn, S.; Chua, R.; Cai, Y.; Kidkhunthod, P.; Manalastas, W. Jr.; Srinivasan, M. Chelating ligands as electrolyte solvent for rechargeable zinc-ion batteries. *Chem. Mater.* **2021**, *33*, 1330–1340.
[47] Nita, C.; Zhang, B.; Dentzer, J.; Ghimbeu, C. M. Hard carbon derived from coconut shells, walnut shells, and corn silk biomass waste exhibiting high capacity for Na-ion batteries. *J. Energy Chem.* **2021**, *58*, 207–218.
[48] Beda, A.; Rabuel, F.; Morcrette, M.; Knopf, S.; Taberna, P. L.; Simon, P.; Ghimbeu, C. M. Hard carbon key properties allow for the achievement of high coulombic efficiency and high volumetric capacity in Na-ion batteries. *J. Mater. Chem. A* **2021**, *9*, 1743–1758.
[49] Ponrouch, A.; Dedryvère, R.; Monti, D.; Demet, A. E.; Mba, J. M. A.; Croguennec, L.; Masquelier, C.; Johansson, P.; Palacín, M. R. Towards high energy density sodium ion batteries through electrolyte optimization. *Energy Environ. Sci.* **2013**, *6*, 2361–2369.
[50] Cai, X.; Zhang, C. P.; Ruan, H. J.; Chen, Z. P.; Zhang, L. J.; Sauer, D. U.; Li, W. H. Cross-scale decoupling kinetic processes in lithium-ion batteries using the multi-dimensional distribution of relaxation time. *Adv. Sci.* **2024**, *11*, 2406934.
[51] Lu, Z. Y.; Geng, C. N.; Yang, H. J.; He, P.; Wu, S. C.; Yang, Q. H.; Zhou, H. S. Step-by-step desolvation enables high-rate and ultra-stable sodium storage in hard carbon anodes. *Proc. Natl. Acad. Sci. USA* **2022**, *119*, e2210203119.
[52] Zhang, T. H.; Xiao, Y.; Zhao, S. S.; Han, Y.; He, G.; Chen, S. M. Manipulating anion solvation competitiveness via a multifunctional additive toward robust low-temperature sodium metal batteries. *Energy Environ. Sci.* **2025**, *18*, 7669–7679.
[53] Li, J. B.; Hao, J. J.; Yuan, Q.; Wang, R. X.; Marlton, F.; Wang, T. Y.; Wang, C. Y.; Guo, X.; Wang, G. X. The effect of salt anion in ether-based electrolyte for electrochemical performance of sodium-ion batteries: A case study of hard carbon. *Carbon Energy* **2024**, *6*, e518.
[54] Wang, C. L.; Thenuwara, A. C.; Luo, J. M.; Shetty, P. P.; McDowell, M. T.; Zhu, H. Y.; Posada-Pérez, S.; Xiong, H.; Hautier, G.; Li, W. Y. Extending the low-temperature operation of sodium metal batteries combining linear and cyclic ether-based electrolyte solutions. *Nat. Commun.* **2022**, *13*, 4934.
[55] Li, J. X.; Sui, S. M.; Zhou, X. Z.; Lei, K. X.; Yang, Q.; Chu, S. X.; Li, L.; Zhao, Y. Q.; Gu, M. J.; Chou, S. L. et al. Weakly coordinating diluent modulated solvation chemistry for high-performance sodium metal batteries. *Angew. Chem., Int. Ed.* **2024**, *63*, e202400406.
[56] Zou, Y. X.; Cheng, F. Y.; Lu, Y.; Xu, Y.; Fang, C.; Han, J. T. High performance low-temperature lithium metal batteries enabled by tailored electrolyte solvation structure. *Small* **2023**, *19*, 2203394.
[57] Zhang, J.; Wang, D. W.; Lv, W.; Zhang, S. W.; Liang, Q. H.; Zheng, D. Q.; Kang, F. Y.; Yang, Q. H. Achieving superb sodium storage performance on carbon anodes through an ether-derived solid electrolyte interphase. *Energy Environ. Sci.* **2017**, *10*, 370–376.

Jiankun Wang obtained his B.Eng. in Chemical Engineering and Technology from Henan Polytechnic University in 2023. He is currently pursuing his Master's degree in Prof. Jieshan Qiu's group at Beijing University of Chemical Technology, with research focusing on hard carbon materials and electrolyte engineering for sodium-ion batteries.

Qi Yang is a professor of College of Chemical Engineering at Beijing University of Chemical Technology. In 2020, he received his Ph.D. degree from City University of Hong Kong. His research focuses on carbon materials, zinc/lithium/sodium-ion batteries, electrochemical engineering, etc.

Zhaodong Huang received his Ph.D. degree in Materials Science and Engineering from the City University of Hong Kong in 2021. He is currently a Research Assistant Professor in the Department of Chemical and Biological Engineering at The Hong Kong University of Science and Technology. His research focuses on advanced materials and electrochemical energy storage devices, with particular interest in lithium-ion, sodium-ion, and zinc-ion batteries, as well as electrolyte engineering.

Jieshan Qiu Cheung-Kong Distinguished Professor, College of Chemical Engineering, Beijing University of Chemical Technology, China. Prof. Qiu is an internationally recognized researcher and thought leader in carbon science and chemical engineering. His research encompasses both fundamental and applied aspects of carbon materials and science, with a focus on the methodologies for producing carbon materials and their applications in energy storage, catalysis, and beyond.